



Computational modeling of turbulent evaporating falling films



Chirag R. Kharangate, Hyoungsoon Lee, Issam Mudawar*

Purdue University Boiling and Two-Phase Flow Laboratory (PU-BTPFL), School of Mechanical Engineering, 585 Purdue Mall, West Lafayette, IN 47907, USA

ARTICLE INFO

Article history:

Received 1 August 2014

Accepted 26 September 2014

Available online 24 October 2014

Keywords:

Falling film

Evaporation

Eddy diffusivity

Computational phase change

ABSTRACT

The primary objective of this study is to construct a computational model for turbulent, free-falling liquid films subjected to evaporative heating. The model is developed for two-dimensional axisymmetric flow on a vertical circular tube, with both the computational domain and operating conditions matching those of an experimental database for evaporating water films. Implemented in FLUENT, the model is used to predict variations of the evaporative heat transfer coefficient along the heated length, as well as profiles of eddy diffusivity, flow velocity, and temperature across the film. Energy transfer at the film's interface is captured successfully with the aid of a prior phase change model. The computational model predicts heat transfer coefficients for a broad range of Reynolds numbers that are in between predictions of two prior experimental correlations. The model predicts eddy diffusivity is fully dampened at the interface. The temperature profile across the liquid film features a steep gradient near the interface, which is attributed to turbulence dampening coupled with energy loss at the film's interface.

© 2014 Published by Elsevier Ltd.

1. Introduction

1.1. Falling-film heat transfer literature

Free-falling liquid films are found in a variety of industries, including chemical, pharmaceutical, and power generation. These films provide high heat transfer coefficients while capitalizing on gravity to achieve liquid motion. Heat exchangers utilizing falling films rely on either sensible or evaporative heating of the film. With sensible heating, the heat absorbed from the wall gradually increases the mean liquid temperature in the flow direction. On the other hand, evaporative heating is achieved once the film's interface reaches saturation temperature. Evaporating liquid films in practical applications are typically turbulent and capitalize upon the added mixing provided by interfacial waves to achieve very attractive heat transfer performance.

Most of the published falling-film studies concern laminar and turbulent fluid flow in adiabatic films. And, while studies concerning heat transfer to films are relatively sparse, far more data are available for sensible heating than evaporation. Table 1 provides a summary of popular falling-film correlations for both sensible heating and evaporative heating derived from measurements by different researchers. For evaporative films, early works include a study by Struve [8], who presented heat transfer data for R11. Chun

and Seban [6] performed fairly extensive measurements of evaporating water films and recommended heat transfer coefficient correlations for both laminar and turbulent films. Fujita and Ueda [9] also performed evaporative heating experiments with water at 1 atmosphere and compared their data to Chun and Seban correlations. Shmerler and Mudawar [7] performed experiments with turbulent free-falling water films and recommended an alternative correlation for the heat transfer coefficient.

1.2. Computational methods for phase change processes

Developing two-phase heat transfer facilities and performing experiments using different fluids and over broad ranges of operating parameters in order to measure heat transfer parameters is a very costly endeavor. This explains the present growing interest in utilizing computational methods to determine the same parameters. Use of computational tools to predict fluid flow and heat transfer in phase change system has been the subject of intense study only during the past two decades. Researchers have suggested different interfacial models to predict mass, momentum and heat transfer in phase change systems. Three main types of phase change models have been widely used for this purpose.

Early works conducted in the 1990s were based on the sharp interface model, which uses the Rankine–Hugoniot jump condition [10] for energy conservation at the interface. Micro-scale mass transfer is neglected and the liquid–vapor interface is maintained at saturation temperature. This allows mass transfer rate to be

* Corresponding author. Tel.: +1 765 494 5705; fax: +1 765 494 0539.

E-mail address: mudawar@ecn.purdue.edu (I. Mudawar).

URL: <https://www.engineering.purdue.edu/BTPFL> (I. Mudawar).

Nomenclature

A^+	constant in eddy diffusivity model	u	local x-direction velocity
E	energy per unit mass	u^*	friction velocity, $\sqrt{\tau_w/\rho_f}$
F	force	x	axial coordinate
g	gravitational acceleration	y	distance perpendicular to the wall
h	heat transfer coefficient	y^+	dimensionless distance perpendicular to the wall, yu^*/ν_f
h_E	heat transfer coefficient for evaporative heating, $q_w''/(T_w - T_{sat})$		
h_E^*	dimensionless heat transfer coefficient for evaporative heating, $h_E \nu_f^{2/3}/(k_f g^{1/3})$	Greek symbols	
h_{fg}	latent heat of vaporization	α	volume fraction, void fraction
h_H	heat transfer coefficient for sensible heating, $q_w''/(T_w - T_m)$	δ	liquid film thickness
h_H^*	dimensionless heat transfer coefficient for sensible heating, $h_H \nu_f^{2/3}/(k_f g^{1/3})$	ε	dissipation rate of turbulent kinetic energy
K	Von-Karman constant	ε_m	eddy momentum diffusivity
k	thermal conductivity; turbulent kinetic energy	ε_h	eddy heat diffusivity
Ka	Kapitza number, $\mu_f^4 g / (\rho_f \sigma^3)$	Γ	mass flow rate per unit film width
L	length of heated portion of test section	γ	accommodation coefficient in Schrage model
M	molecular weight	μ	dynamic viscosity
\dot{m}''	interfacial mass flux	ν	kinematic viscosity
\vec{n}	unit vector normal to interface	ρ	density
p	pressure	τ	shear stress
Pr	Prandtl number		
$Pr_{f,T}$	turbulent Prandtl number	Superscripts	
Q	energy source term	\rightarrow	vector
q''	local heat flux normal to the wall	$+$	dimensionless
q_w''	wall heat flux		
R	universal gas constant (8.314 J/mol K)	Subscripts	
r	radial coordinate	c	condensation
Re	Reynolds number, $4\Gamma/\mu_f$	$crit$	critical
r_i	mass transfer intensity factor	e	evaporation
S	volumetric mass source term	eff	effective
T	temperature	f	liquid
t	time	g	vapor
T_{sat}	saturation temperature	i	interfacial
		m	mean
		sat	saturation
		w	wall

determined from energy conservation at the interface according to the relation

$$q_i'' = -k_{eff} \nabla T_i \cdot \vec{n} = \dot{m}'' h_{fg}, \quad (1)$$

where \dot{m}'' [kg/m² s] is the mass flux due to phase change at the interface. The volumetric mass source term, S [kg/m³ s], for the individual phases is determined from

$$S_g = -S_f = \dot{m}'' |\nabla \alpha_g| = \frac{k_{eff} (\nabla \alpha \cdot \nabla T)}{h_{fg}}, \quad (2)$$

where k_{eff} is the effective thermal conductivity determined from the volume fractions and thermal conductivities of the liquid and vapor. In effect, this model uses all energy crossing the interface for mass transfer.

The second popular approach is based on a model by Schrage [11], which in turn is based on the Hertz–Knudsen equation [12] that allows for interfacial jump in temperature and pressure, where $T_{sat}(p_f) = T_f \neq T_{sat}(p_g) = T_g$. The net mass flux across the interface, \dot{m}'' [kg/m² s], is determined by the difference between liquid to vapor and vapor to liquid mass fluxes,

$$\dot{m}'' = \frac{2}{2 - \gamma_c} \sqrt{\frac{M}{2\pi R}} \left(\gamma_c \frac{P_g}{\sqrt{T_g}} - \gamma_e \frac{P_f}{\sqrt{T_f}} \right), \quad (3)$$

where $R = 8.314$ J/mol K is universal gas constant, γ the fraction of molecules transferred from one phase to the other during phase

change, and $1 - \gamma$ the fraction of molecules reflected at the interface. The subscripts c and e in Eq. (3) refer to condensation and evaporation, respectively, and $\gamma_e = 1$ and $\gamma_c = 1$ represent complete evaporation and complete condensation, respectively [13]. Many investigators use equal values of γ_c and γ_e by setting $\gamma_c = \gamma_e = \gamma$ in phase change simulations, and refer to γ as the “accommodation coefficient”. Tanasawa [14] simplified Eq. (3) by setting the interfacial temperature equal to T_{sat} , and assuming the heat flux is linearly dependent on temperature jump between the interface and the vapor. For evaporation, their modified model is expressed as

$$\dot{m}'' = \frac{2\gamma}{2 - \gamma} \sqrt{\frac{M}{2\pi R}} \frac{\rho_g h_{fg} (T - T_{sat})}{T_{sat}^{3/2}}, \quad (4)$$

where T_{sat} is based on local pressure, p , and the volumetric mass source term is determined from

$$S_g = -S_f = \dot{m}'' |\nabla \alpha_g|. \quad (5)$$

This model is applicable only to the liquid–vapor interface, and has been used mostly to tackle evaporating and condensing films, and film boiling.

The third popular approach is based on a phase change model proposed by Lee [15]. This model has been widely used in condensation studies, but is applicable to both condensation and boiling. The Lee model is based on the assumption that mass is transferred

Table 1
Heat transfer coefficient correlations for falling films.

Author(s)	Correlation	Range
Sensible heating Wilke [1]	$h_{ii}^* = 2.07Re^{-1/3}$	$Re < 2460Pr_f^{-0.646}$
	$h_{ii}^* = 0.0323Re^{1/5}Pr_f^{0.344}$	$2460Pr_f^{-0.646} < Re < 1600$
	$h_{ii}^* = 0.00102Re^{2/3}Pr_f^{0.344}$	$1600 < Re < 3200$
	$h_{ii}^* = 0.00871Re^{2/5}Pr_f^{0.344}$	$3200 < Re$
Gimbutis [2]	$h_{ii}^* = (0.165Re^{0.16} - 0.4)Pr_f^{0.34} \left(\frac{Pr_L}{Pr_{f,w}}\right)^{0.25}$	$2800 \leq Re \leq 70,000$ $4.3 < Pr_f < 8.4$
Shmerler and Mudawar [3]	$h_{ii}^* = 0.0106Re^{0.3}Pr_f^{0.63}$	$2500 \leq Re \leq 39,500$ $2.55 < Pr_f < 6.87$
Al-Najem et al. [4]	$h_{ii}^* = 6.832 \times 10^{-4} \left(Re^{0.4829} Pr_f^{0.93717} - \frac{21.817.84}{Re} \right)$	$4000 \leq Re \leq 20,000$ $1.8 < Pr_f < 4.4$
Ye et al. [5]	$h_{ii}^* = 0.00462Re^{0.429}Pr_f^{1/3}$	$800 \leq Re \leq 7000$ $2.55 < Pr_f < 7.2$
Evaporative heating Chun and Seban [6]	$h_E^* = 0.0038Re^{0.4}Pr_f^{0.65}$	$320 \leq Re \leq 21,000$ $1.77 < Pr_f < 5.7$
	$h_E^* = 0.0038Re^{0.35}Pr_f^{0.95}$	$4990 < Re < 37,620$ $1.75 < Pr_f < 5.42$

at a constant pressure and a quasi thermo-equilibrium state, and obtained from the relations

$$S_g = -S_f = r_i \alpha_g \rho_g \frac{(T - T_{sat})}{T_{sat}} \text{ for condensation } (T < T_{sat}) \quad (6a)$$

and

$$S_g = -S_f = r_i \alpha_f \rho_f \frac{(T - T_{sat})}{T_{sat}} \text{ for evaporation } (T > T_{sat}), \quad (6b)$$

where r_i is an empirical coefficient called the “mass-transfer intensity factor”, and has the units of s^{-1} . This model is the least physical of the three models but has the simplest form. Eqs. (6a) and (6b) reveal that this model relies on some form of weighting factor to determine mass transfer. It is important to note that the Lee model does not set physical limits on the coefficient r_i . With this model, phase change is defined both at the liquid–vapor interface and the phase being changed, i.e., liquid phase for boiling and vapor phase for condensation.

1.3. Objectives of study

The primary objective of the present study is to develop a computational model for evaporating turbulent free-falling liquid films. An appropriate phase change model will be adapted to predict the fluid flow and heat transfer characteristics of the film. The predictive accuracy of the model will be assessed against data for water corresponding to a broad range of Reynolds numbers. The computational model is used to generate eddy diffusivity, velocity and temperature profiles across the film. Another objective of this study is to help lay a foundation for future computational modeling of boiling and condensation processes.

2. Experimental methods

The data used to assess the accuracy of the computational model are obtained using the Purdue University Boiling and Two-Phase Flow Laboratory (PU-BTPFL) falling-film facility depicted in Fig. 1(a). Fig. 1(b) shows a schematic diagram of the flow loop that

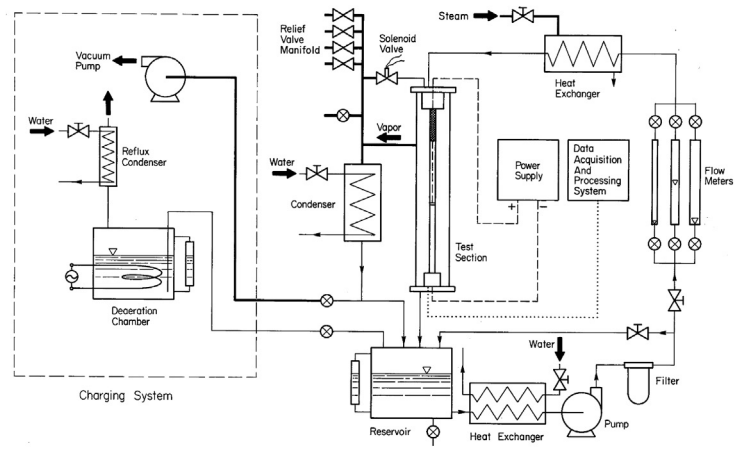
delivered deionized water at the desired flow rate, pressure and temperature to a test chamber containing the falling-film test section. Fluid purity plays a paramount role in this study, and is achieved using the charging system depicted in Fig. 1(b). A vacuum pump is used first to remove any fluid from the loop. The water is then deaerated by vigorous boiling before being charged into the loop’s reservoir. During the tests, the water is circulated by a magnetically coupled centrifugal pump, with the pressure and flow rate regulated with the aid of a control valve and a bypass valve. Temperature is regulated with the aid of two separate heat exchangers.

Fig. 2(a) shows the construction of the test chamber. The liquid film is formed on the outer surface of a vertical 25.4-mm diameter, 1835-mm long cylindrical test section contained in a leak proof chamber made from Lexgard plastic. The chamber is comprised of two identical flanged sections with outer dimensions of $152.5 \times 152.5 \times 991 \text{ mm}^3$ and a wall thickness of 35 mm. The test section consists of three parts: a 300-mm long porous polyethylene tube, a 757-mm long G-10 fiberglass plastic tube, and a 781-mm long stainless steel tube. The water flows radially outwards from an inlet reservoir through the porous wall of the polyethylene tube before falling downwards as a thin film along the outer walls of the downstream fiberglass plastic and stainless steel tubes. The polyethylene tube has a mean porosity of 20 μm , which causes the water film to be formed gradually and uniformly with minimal radial velocity. The middle, adiabatic G-10 tube allows the film to be develop hydrodynamically before being heated along the lower stainless steel tube. Soldered to the upper and lower ends of the stainless steel tube are short copper cylinders that serve as electrical terminals. Low voltage, high d.c. current (up to 15 V and 750 A) is passed across the copper terminals through the 0.41-mm thick wall of the stainless steel tube, generating a uniform heat flux along the outer wall of the same tube. The wall heat flux is maintained at least 25% below the onset of nucleate boiling.

Wall temperature of the stainless steel tube is measured by diametrically opposite pairs of type-T thermocouples at 17 axial locations. Thermal entrance effects are captured by reducing the axial pitch of thermocouples near the top of the stainless steel tube. Fig. 2(b) shows the provisions adopted to obtain accurate inner

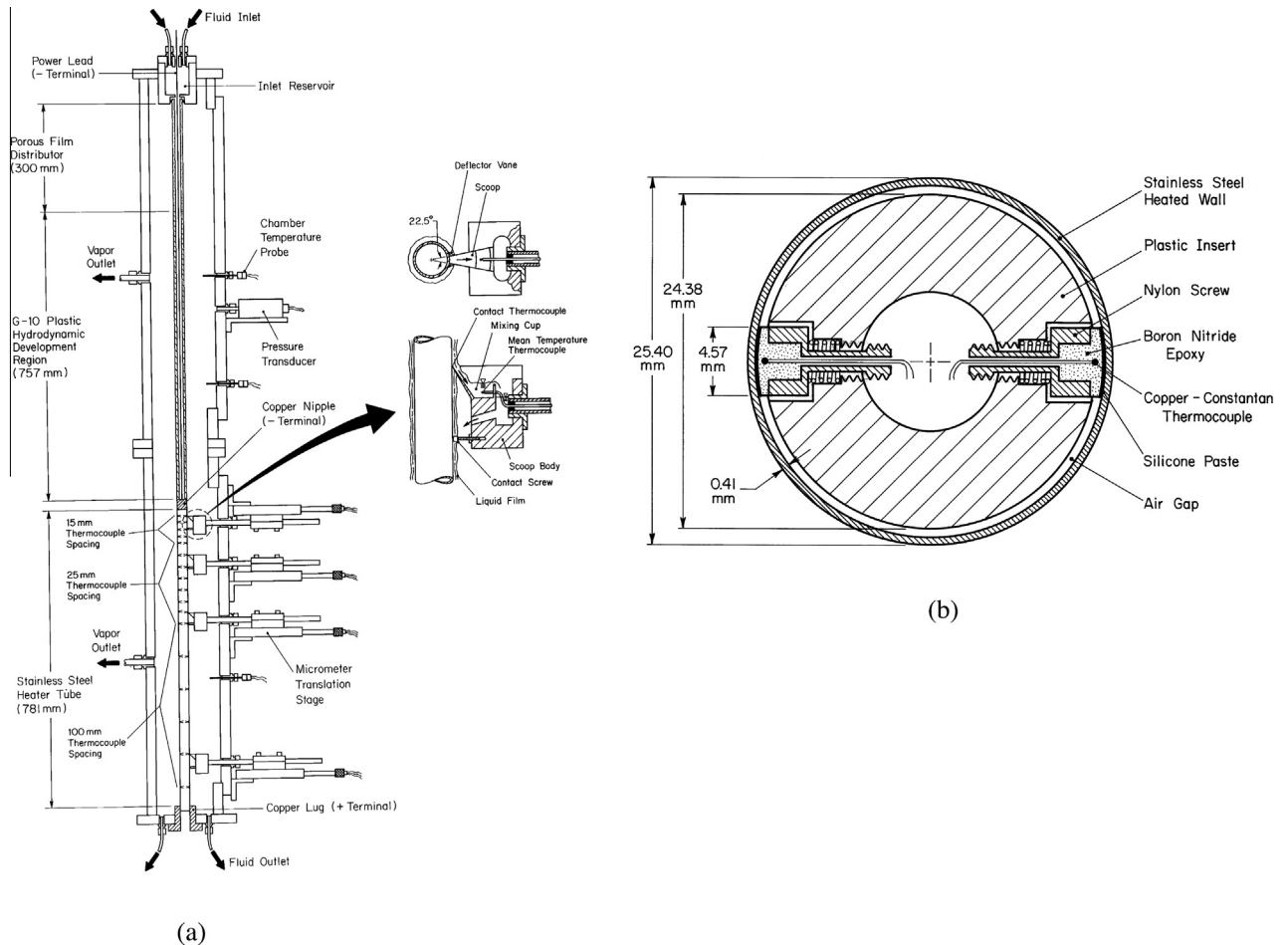


(a)



(b)

Fig. 1. (a) Photo of falling film facility. (b) Schematic diagram of flow loop.



(a)

(b)

Fig. 2. (a) Cut-away view of test chamber. (b) Cross-sectional view of inner wall thermocouples.

wall temperature measurements. The bead of each thermocouple is embedded in a small mass of thermally conducting boron nitride epoxy that is deposited into the head of a 6–32 nylon socket head cap screw. The epoxy is machined to a cylindrical profile to match the inner surface of the stainless steel tube. The threads of the nylon screw closest to the head are machined out in order to insert a stainless steel spring, while a few threads on the opposite end of the screw are retained for insertion into a Delrin plastic tube that is slid along the inside of the stainless tube, allowing the screw to be compressed normal to the axis of the Delrin tube. During assembly, the screw heads are painted with a thin layer of thermally conducting silicone grease, then each diametrically opposite pair is compressed inwards for insertion into the stainless steel tube. The spring forces the boron nitride epoxy to make precise contact with the inner wall of the stainless steel tube. This process is repeated for each thermocouples pair as the Delrin tube is slid gradually along the stainless steel tube.

3. Computational methods

3.1. Computational domain

Fig. 3 shows the domain used in the computational model. Because of the symmetrical construction of the test section and small ratio of film thickness to distance between the test section and test chamber walls, the flow is assumed axisymmetric and two-dimensional. The computational domain consists of the inlet reservoir, porous film distributor, and 1835-mm long annulus formed between the outer wall of the 25.4-mm test section and Lexgard chamber. FLUENT Analysis System in the Toolbox of ANSYS Workbench 12.1 [16] is used to compute the fluid flow and heat transfer parameters. The complete analysis is performed in the Project Schematic of Workbench, including geometry creation, meshing, processing and post-processing.

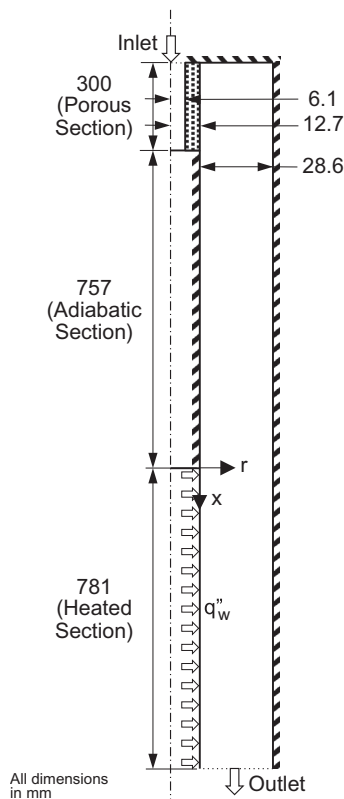


Fig. 3. Computational domain.

3.2. Governing equations

The present model employs the standard two-equation $k-\omega$ turbulent model with shear stress transport (SST) formulation as prescribed in the ANSYS Guide [16]. A key reason for using the $k-\omega$ model is its ability to tackle turbulence dampening at the interface, which is key to obtaining accurate temperature profiles adjacent to the interface, a feature not available with other models, such as the popular $k-\varepsilon$ model. A turbulence dampening factor of 10 is prescribed. Two-phase treatment follows the Volume of Fluid (VOF) model [17], and solid–liquid interfaces are governed by continuities of both temperature and heat flux. The VOF model in FLUENT is used to compute conservation equations for liquid and vapor while also accounting for mass transfer between the two phases. The continuity equations are expressed as [16]

$$\text{liquid phase : } \frac{\partial}{\partial t} (\alpha_f \rho_f) + \nabla \cdot (\alpha_f \rho_f \vec{u}_f) = S_f, \quad (7a)$$

$$\text{vapor phase : } \frac{\partial}{\partial t} (\alpha_g \rho_g) + \nabla \cdot (\alpha_g \rho_g \vec{u}_g) = S_g. \quad (7b)$$

The momentum and energy equations, which are applied to the combined phases, are expressed, respectively, as

$$\begin{aligned} \text{momentum : } & \frac{\partial}{\partial t} (\rho \vec{u}) + \nabla \cdot (\rho \vec{u} \vec{u}) \\ & = -\nabla P + \nabla \cdot [\mu (\nabla \vec{u} + \nabla \vec{u}^T)] + \rho \vec{g} + \vec{F}, \end{aligned} \quad (8)$$

$$\text{energy : } \frac{\partial}{\partial t} (\rho E) + \nabla \cdot (\vec{u} (\rho E + P)) = \nabla \cdot (k_{eff} \nabla T) + Q. \quad (9)$$

where E [J/kg] is the energy per unit mass, which is determined from

$$E = \frac{\alpha_f \rho_f E_f + \alpha_g \rho_g E_g}{\alpha_f \rho_f + \alpha_g \rho_g}, \quad (10)$$

$$\text{where } \rho = \alpha_f \rho_f + \alpha_g \rho_g, \quad (11a)$$

$$\mu = \alpha_f \mu_f + \alpha_g \mu_g, \quad (11b)$$

$$\text{and } k_{eff} = \alpha_f k_f + \alpha_g k_g. \quad (11c)$$

In the present computations, mass transfer due to evaporation is accounted for by using the appropriate mass source terms, S_f and S_g , and the corresponding energy transfer term is accounted for as

$$Q = h_{fg} S_f. \quad (12)$$

3.3. Phase change model

The phase change model by Lee [15] commonly used with boiling and condensation situations attempts to maintain saturation conditions at the interface while allowing for mass and energy transfer in one of the phases. Physically, use of α_k multipliers in Eqs. (6a) and (6b) implies that it is possible for mass transfer to occur where phase k exists as long as the temperature condition is satisfied. Fig. 4(a) shows the region where the source term is valid when using the Lee model for evaporation. Notice that phase change is allowed in the liquid phase and at the interface when $T > T_{sat}$. However, this is not physically what is expected in an evaporating falling film. By maintaining the wall heat flux at least 25% below the onset of boiling, phase change will take place at the film's interface but nowhere else within the liquid domain.

The sharp interface model and Tanasawa model [14] (which is a simplified form of the Schrage [11] model) are better suited to the present situation because they allow mass transfer to occur only at

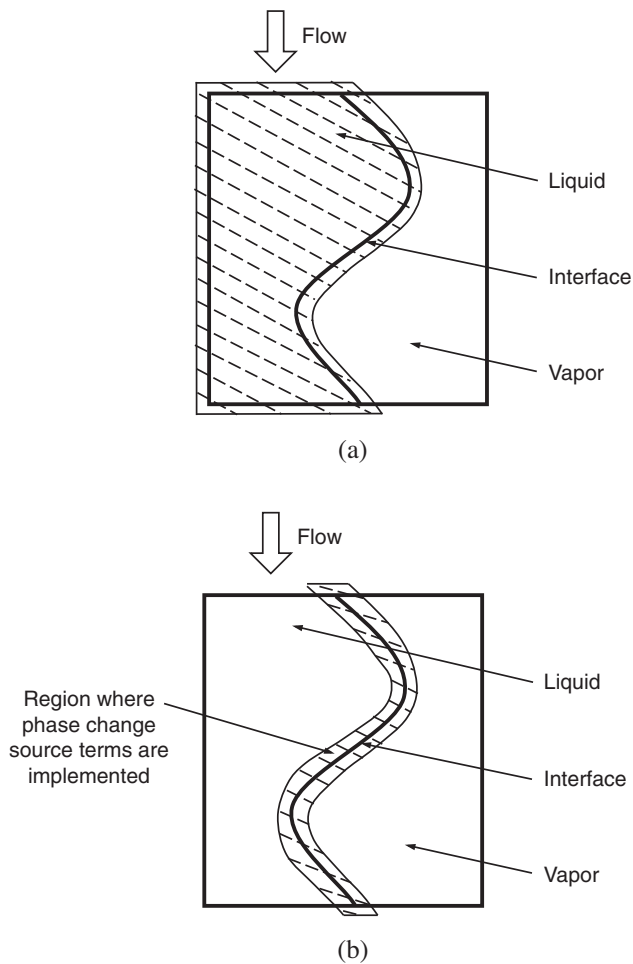


Fig. 4. Differences in enforcement of phase change source terms during evaporation using (a) Lee model [15], and (b) sharp interface and Tanasawa models [14].

the interface. Fig. 4(b) shows where the source terms are valid when using the sharp interface model and Tanasawa model for evaporation. This domain is the result of the $\nabla\alpha_g$ multiplier yielding non-zero source terms in Eqs. (2) and (5) only at the interface. The sharp interface model converts any energy crossing the interface to phase change; this energy is not defined by the problem but realized in the solution. This solution can be different for different situations depending on how much energy crosses the interface versus being carried away by the liquid. What is being sought in the present evaporating film situation is the ability to predict and specify this energy so that T_{sat} is maintained at the interface. The sharp interface model can be utilized here if the temperatures of the interface and surrounding vapor are manually maintained at T_{sat} , or if energy transfer is confined to the interface with the vapor temperature maintained at T_{sat} . On the other hand, Tanasawa's model does not require placing any of these restrictions for the present situation, and is therefore the most convenient option, provided an appropriate value of γ is used. The Tanasawa's model is therefore adopted in all the present computations. Marek and Straub [13] determined the value of γ based on published data. They recommended $\gamma = 0.1$ –1 for dynamically renewing water surfaces such as jets or moving films, and $\gamma < 0.1$ for stagnant surfaces. Hardt and Wondra [18] set $\gamma = 1$ for film boiling, and Magnini et al. [19] also set $\gamma = 1$ for laminar flow boiling based on a recommendation by Rose [20]. On the other hand, Kartuzova and Kassemi [21] used a relatively low value of $\gamma = 0.01$ in their simulation of ventless pressurization of a cryogenic storage tank.

It is observed that a low value of γ yields interfacial temperatures higher than T_{sat} . After testing different values of γ in the present study, it is determined that $\gamma = 0.1$ helps maintain interfacial temperature at T_{sat} with reasonable accuracy. It is also worth noting that some of the cases examined here are successfully modeled with γ values as high as 1, but these results are realized at the expense of reduced stability of the numerical solution. On the other hand, $\gamma < 0.1$ resulted in deviation of interfacial temperature from T_{sat} for several cases. Therefore, a constant value of $\gamma = 0.1$ is deemed most appropriate based on its ability to maintain interfacial temperature at $T_{sat} \pm 0.1$ °C for all test cases. Another reason for using this small value of γ is that it requires minimal energy to maintain T_{sat} . Using $\gamma = 0.1$, the mass flux obtained from Eq. (4) is used to calculate the mass source terms, S_g and S_f , according to Eq. (5), and the corresponding energy source term due to evaporation, Q [W/m³], according to Eq. (12).

3.4. Grid size

The grid system used in the present study consists of 1,397,474 nodes and 1,467,562 cells. Two finer grid systems, with 2,273,821 and 3,057,589 cells, were attempted and found to provide minimal influence on the computed results. The grid used is non-uniform, having greater density in the porous zone and near the wall and film interface, especially for the heated portion of the test section, in pursuit of superior accuracy in resolving key flow parameters. Turbulence is captured accurately near the wall by using a minimum of five cells within $y^+ < 5$.

4. Computational results

4.1. Interfacial waves

Interfacial waviness is an inherent feature of falling liquid films that influences mass, momentum and heat transfer characteristics.

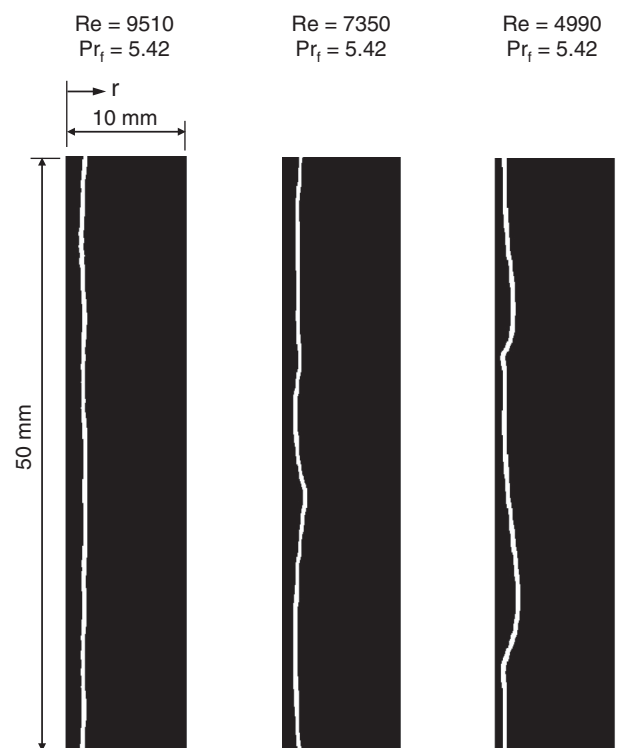


Fig. 5. Interfacial waves at axial distance centered 0.75 m from inlet of heated length for three Reynolds numbers and $Pr_f = 5.42$.

The waves can be assessed by examining both the temporal and spatial variations of the film thickness. The present computations are performed for film Reynolds numbers of $Re = 4990–37,620$ and Prandtl numbers of $Pr_f = 1.75–5.42$. Most cases are successfully modeled except those associated with low Re and low Pr_f numbers. At lower Pr_f numbers, it is found that it is very difficult to create the film for smaller Re cases. Hence, only 10 of the 13 cases tested yielded convergent solutions.

Fig. 5 shows instantaneous film profiles for three different Re values and $Pr_f = 5.42$. Notice that the average film thickness decreases with decreasing Re . The highest Re case also features a well-defined film substrate with the interface potentially masking high frequency perturbations. On the other hand, the lowest Re case shows more pronounced long waves with large fluctuations in substrate thickness. It should be noted that film formation at lower Re , especially for the lowest Pr_f of 1.75, is both more difficult to compute and prone to appreciable film breakup.

4.2. Heat transfer coefficient

The evaporation heat transfer coefficient is computed using local time averaged values of

$$h_E(x) = \frac{1}{\Delta t(x)} \int_0^{\Delta t(x)} h_E(x, t) dt. \tag{13}$$

The period Δt is carefully chosen to include at least 30 periods of the dominant film profile. After a steady film is formed, it is observed that a 0.2-s period is sufficient to provide repeatable heat transfer values as explained in a recent study by Mascarenhas and Mudawar [22] involving turbulent falling films subjected to sensible heating. Fig. 6(a)–(d) shows axial variations of the dimensionless evaporation heat transfer coefficient,

$$h_E^* = \frac{h_E v_f^{2/3}}{k_f g^{1/3}}, \tag{14}$$

along the heated length for different Reynolds numbers and $Pr_f = 1.72, 3.07, 4.52$ and 5.42 , respectively. For each combination of Re and Pr_f , the plots show the experimental data, curve fit to the experimental data, and computed variations. For all cases, the data show a thermal development region persisting to over one half the heated length. Thermal development lengths are also evident in the computed variations, but they are prolonged for most cases compared to the data. Lack of a clearly defined downstream fully developed region is attributed to the inability of the phase change model to accurately account for interfacial energy transfer. Different values of γ in Eq. (4) provide different mass fluxes and therefore different energy transfer rates at the interface.

These results bring into question the choice of optimum value of γ as discussed earlier. A constant value of $\gamma = 0.1$ is used in the

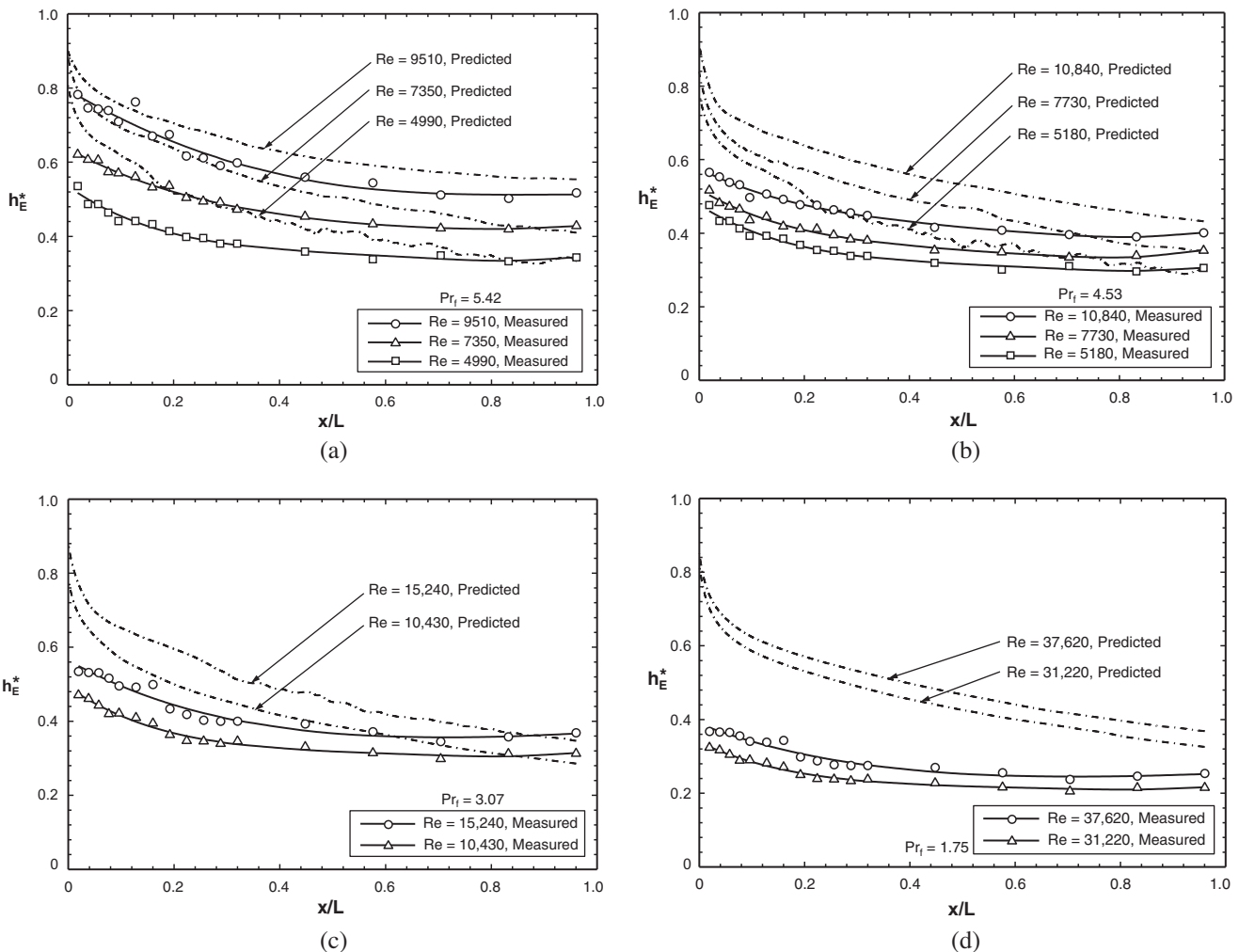


Fig. 6. Variations of measured and predicted dimensionless heat transfer coefficients along heated length of test section for different Reynolds numbers and (a) $Pr_f = 5.42$, (b) $Pr_f = 4.53$, (c) $Pr_f = 3.07$, and (d) $Pr_f = 1.75$.

present study to achieve both numerical stability and uniformity in solution method. But using a constant value might be responsible, at least in part, for the prolonged thermal entrance lengths in the computed variations in Fig. 6(a)–(d).

Notice also that there is some departure between predicted and measured values in the upstream part of the thermal development region. The predicted values show a steeper drop near $x = 0$, compared to a milder drop for the experimental data. This difference might be related to the design of the test section, specifically at $x = 0$ and $x = L$, where the stainless steel tube is soldered to short copper cylinders that act as electrical terminals for the current supplied through the stainless steel wall. Axial heat conduction along the stainless steel wall towards the terminal blocks compromise the uniformity of wall heat flux at these locations and mask the sharp drop in wall temperature near $x = 0$. Overall, the computed results show reasonable agreement for the $Pr_f = 3.07, 4.52$ and 5.43 cases, but appreciable departure for the lowest $Pr = 1.72$ cases, where liquid viscosity is lowest. These results indicate that the model is less successful in tackling the highest temperature case.

The developing nature of the film makes it difficult to determine a universal correlation for the fully developed evaporation heat transfer coefficient. Shmerler and Mudawar [7] determined fully developed h_E^* by averaging values measured at $x/L = 0.576, 0.704$ and 0.832 , outside the upstream thermal development region and the exit region. Using the same axial range of $x/L = 0.576–0.832$,

the computed values are spatially averaged to yield the following dimensionless relation for “fully developed” evaporation heat transfer coefficient,

$$h_E^* = 0.00044 Re^{0.598} Pr_f^{0.975}, \tag{15}$$

as shown in Fig. 7(a), where all fluid properties are based on saturation conditions. Fig. 7(b) shows this relation falling mostly between the correlations of Chun and Seban [6], and Shmerler and Mudawar [7].

4.3. Eddy diffusivity and velocity profiles

Analytical modeling of the film’s fluid flow and heat transfer depends highly on the ability to accurately model turbulence structure across the film. Turbulence effects are reflected in the variation of eddy momentum diffusivity, ϵ_m , and eddy heat diffusivity, ϵ_h , across the film. For a turbulent falling film, the variations of shear stress and heat flux across the film are expressed as

$$\tau = \mu_f \left(1 + \frac{\epsilon_m}{\nu_f} \right) \frac{\partial u}{\partial y} \tag{16}$$

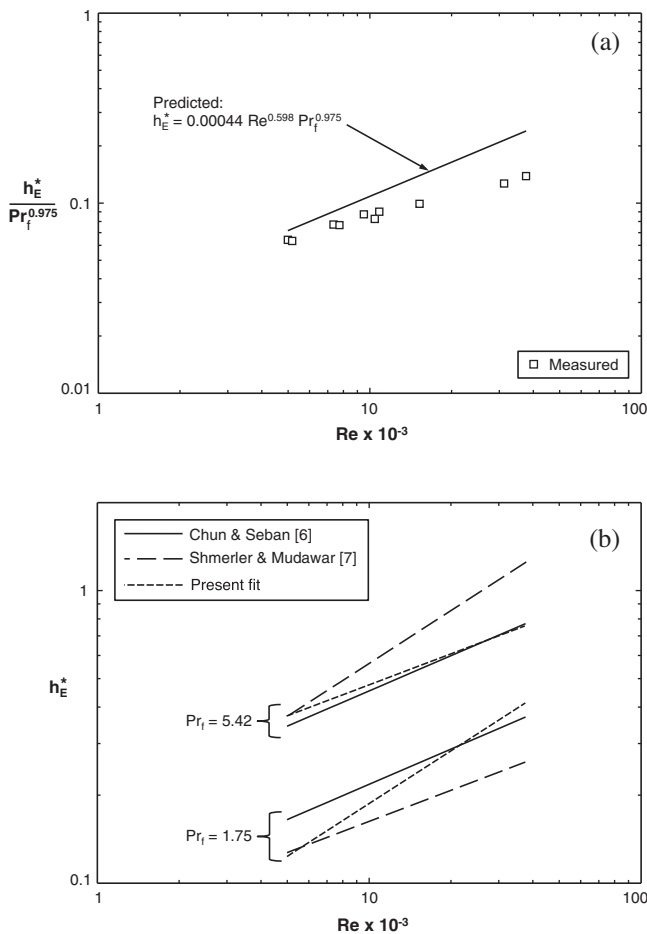


Fig. 7. (a) Comparison of measured and computed variations of dimensionless fully-developed evaporation heat transfer coefficient with Reynolds number for $Re = 4990–37,620$ and $Pr_f = 1.75–5.42$. (b) Comparison of computed variation of dimensionless fully-developed evaporation heat transfer coefficient with prior correlations for $Pr_f = 1.75$ and 5.42 .

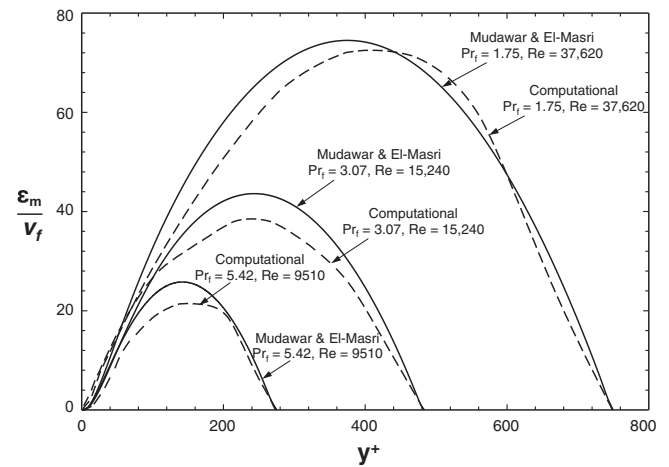


Fig. 8. Comparison of predicted eddy diffusivity profiles with Mudawar and El-Masri’s [29] at axial distance 0.75 m from inlet of heated length for different Reynolds and Prandtl numbers.

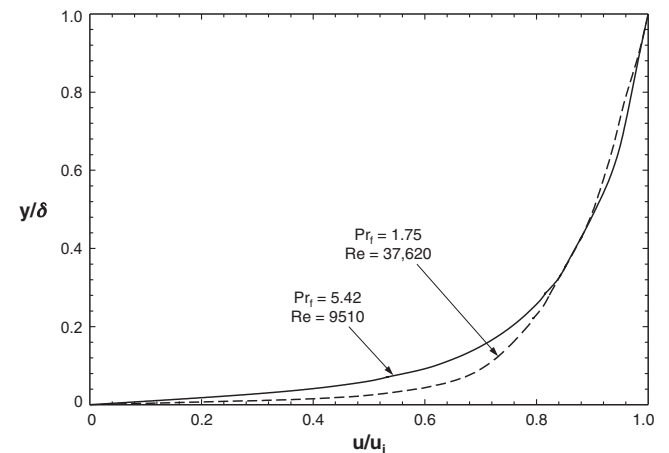


Fig. 9. Computed x -velocity profiles at axial distance 0.75 m from inlet to heated length for $Re = 9510$ and $Pr_f = 5.42$, and $Re = 37,620$ and $Pr_f = 1.75$.

and

$$q'' = -k_f \left(1 + \frac{Pr_f}{Pr_{f,T}} \frac{\epsilon_m}{\nu_f} \right) \frac{\partial T}{\partial y}, \tag{17}$$

where $Pr_{f,T} = \epsilon_m / \epsilon_h$ is the turbulent Prandtl number.

Eddy diffusivity across a turbulent boundary layer is often modeled with the aid of a modified Van Driest formulation [23]. But eddy diffusivity profiles commonly utilized with internal or external flows single-phase flows [24,25] lack the ability to account for the dampening influence of surface tension on turbulence eddies near a liquid–vapor interface. Mills and Chung [26], Seban and Faghri [27], Hubbard et al. [28], and Mudawar and El-Masri [29] recommended different formulations to account for the dampening of eddy diffusivity near the interface. Mudawar and El-Masri developed a single continuous eddy diffusivity profile incorporating the Van Driest model near the wall, an experimental profile derived from open channel flow data for the bulk region of the film, and a dampening multiplier for the interface region. The Mudawar and El-Masri profile is given by

$$\frac{\epsilon_m}{\nu_f} = -\frac{1}{2} + \frac{1}{2} \sqrt{1 + 4K^2 (y^+)^2 \left(1 - \frac{y^+}{\delta^+} \right)^2 \left[1 - \exp \left\{ -\frac{y^+}{A^+} \left(1 - \frac{y^+}{\delta^+} \right)^{1/2} \left(1 - \frac{0.865 Re_{crit}^{1/2}}{\delta^+} \right) \right\} \right]^2}, \tag{18}$$

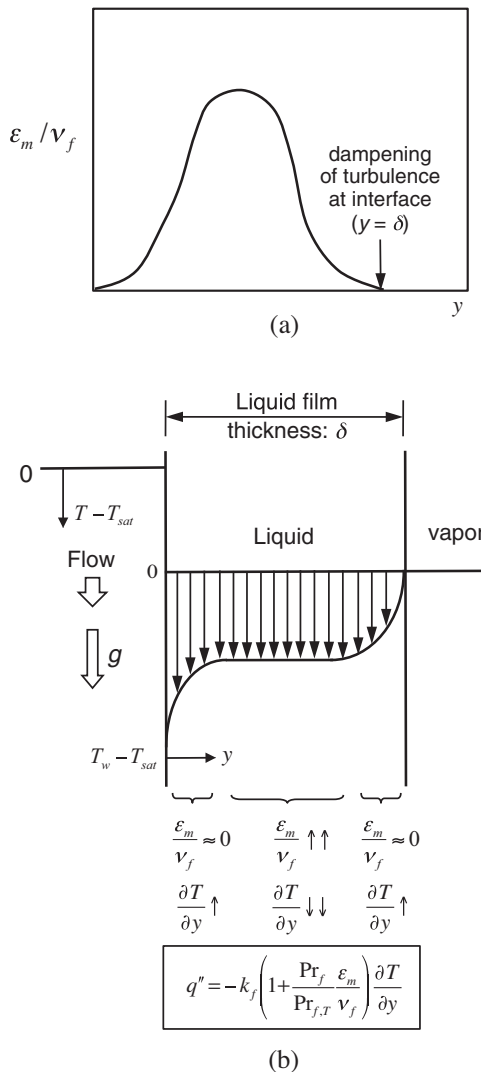


Fig. 10. Schematic representations of (a) eddy momentum diffusivity profile across the liquid film, and (b) influence of interfacial dampening of eddy momentum diffusivity on temperature profile.

where $K = 0.4$, $A^+ = 26$, and $Re_{crit} = 97 / Ka^{0.1}$ for sensible heating or $Re_{crit} = 0.04 / Ka^{0.37}$ for evaporative heating. They also recommended the following relation for turbulent Prandtl number,

$$Pr_{f,T} = 0.66 + 1.4 \exp \left(-15 \frac{y^+}{\delta^+} \right). \tag{19}$$

Fig. 8 compares the average eddy diffusivity profile across the film at an axial location of $x = 0.75$ m from the inlet of the heated length determined from the computational model with the Mudawar and El-Masri profile for three different cases. The average profile is obtained by averaging eddy diffusivity profiles for different subintervals within a period of a single dominant wave, as explained by Mascarenhas and Mudawar [22] for turbulent falling films subjected to sensible heating. Notice that, like the empirical profile, the computed eddy diffusivity is zero both at the wall and the film interface. There is also good overall agreement between the computed and empirical profiles in both shape and magnitude, evidenced by R -square fits of 0.96, 0.92 and 0.88 for $Re = 37,620$ and $Pr_f = 1.75$, $Re = 15,240$ and $Pr_f = 3.07$, and $Re = 9510$ and $Pr_f = 5.42$, respectively. These trends are also similar to those of the eddy diffusivity profiles computed by Mascarenhas and Mudawar for sensible heating.

Fig. 9 shows x -velocity profiles across the film computed at $x = 0.75$ m for two cases: $Re = 37,620$ and $Pr_f = 1.75$, and $Re = 9510$ and $Pr_f = 5.42$. These profiles are representative of turbulent boundary layer profiles with the higher velocity displaying steeper slope near the wall.

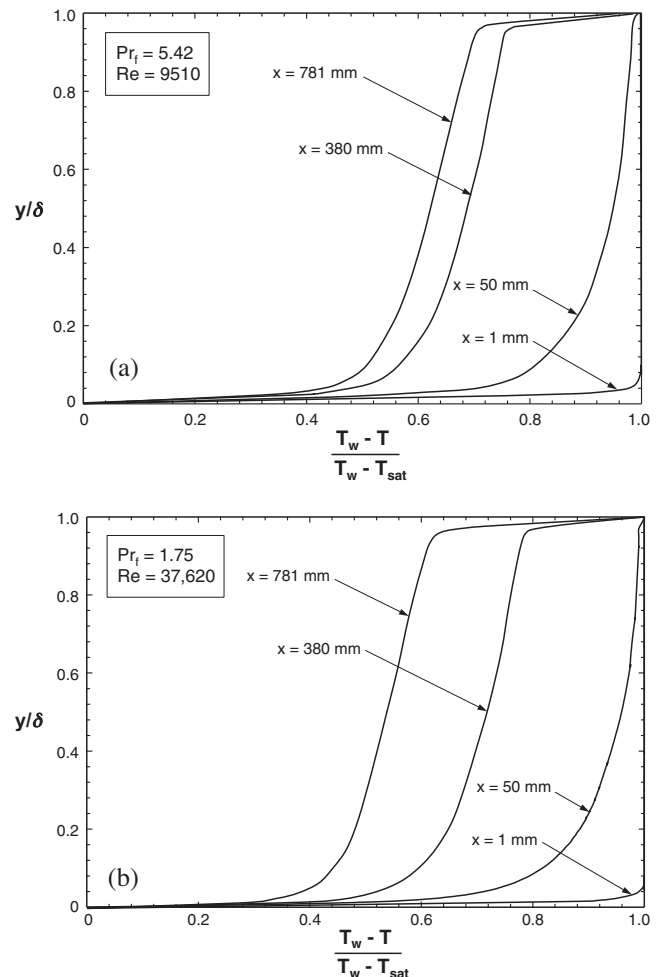


Fig. 11. Predicted development of temperature profiles along heated length for (a) $Re = 9510$ and $Pr_f = 5.42$, and (b) $Re = 37,620$ and $Pr_f = 1.75$.

4.4. Temperature profile

Eddy diffusivity and $Pr_{f,T}$ are also essential for analytical determination of temperature profile across the film. For a thermally fully developed film, the heat flux across the film is constant and equal to the wall heat flux, q''_w . Eq. (17) shows that, at least for the fully developed region, temperature profile across the film acquires a large slope where ϵ_m/ν_f tends to zero, and a small slope where ϵ_m/ν_f tends to a maximum. This behavior is explained with the aid of Fig. 10(a) and (b). An eddy diffusivity profile is shown in Fig. 10(a) having zero values both at the wall and the interface, and a maximum somewhere in between, as depicted earlier in Fig. 8. Fig. 10(b) shows the temperature profile acquires large slope both at the wall, where $T = T_w$, and the interface, where $T = T_{sat}$. The temperature profile displays an unusual temperature gradient at the interface, which is not commonly observed with turbulent thermal boundary layers for other flow situations.

Fig. 11(a) and (b) depict computed non-dimensional temperature profiles across the liquid film computed at four axial locations for $Re = 9510$ and $Pr_f = 5.42$, and $Re = 37,620$ and $Pr_f = 1.75$, respectively. The phase change model employed in this study is clearly capable of capturing the aforementioned temperature profile trends. Notice how the temperature profile features a sharp gradient near the interface, implying a finite heat flux is dissipated at the interface, and that the computed interface temperature is very close to T_{sat} . Additionally, the gradient near the interface is shown increasing axially, which suggests a larger fraction of the wall heat flux is being dissipated at the interface as the film flows downstream. These trends demonstrate that the phase change model adopted in this study is able to replicate the physical phenomena quite well. It is worth indicating that the same phase change model would have failed to capture the interfacial temperature gradient without the dampening of eddy diffusivity at the interface. On the other hand, the interfacial temperature gradient can be achieved without the complete dampening of eddy diffusivity at

the interface if the heat flux at the interface is artificially increased. However, following the minimum energy principle, it is physically more realistic if the eddy diffusivity is a minimum.

Overall, these facts and temperature trends prove that the two-equation $k-\omega$ turbulent model, with shear stress transport (SST) formulation and a turbulence dampening factor of 10, is able to capture all the physical phenomena quite well, and therefore well suited for turbulent evaporating falling films.

The influence of interfacial dampening of eddy diffusivity is reflected in fundamental differences between sensible and evaporative heating of turbulent falling films. For sensible heating, the wall heat flux is absorbed by the film rather than dissipated at the interface. With a small heat flux at the interface, Eq. (17) indicated that the temperature profile will not acquire a steep gradient at the interface where ϵ_m/ν_f tends to zero. Fig. 12 highlights the differences between temperature profiles for sensible and evaporative heating of turbulent falling films along the heated length. Sensible heating is shown yielding a steep gradient at the wall but not at the interface. Whereas, evaporative heating is shown yielding steep gradients both at the wall and the interface. Once the evaporating film becomes thermally fully developed, it is able to transfer all the wall energy across the film and to the interface without increasing the wall or film temperatures.

4.5. Future work

The present study provides valuable insight into fluid flow and heat transfer behavior as well as turbulent characteristics of an evaporating free-falling film. However, validation of both computational and analytical models can benefit greatly from future detailed measurements of film thickness, liquid velocity and liquid temperature. Previous studies on adiabatic, relatively thick films [30,31] provide a framework for future simultaneous measurements of interfacial waves and turbulence structure. Given the small thickness of falling films, miniaturized diagnostic tools, such

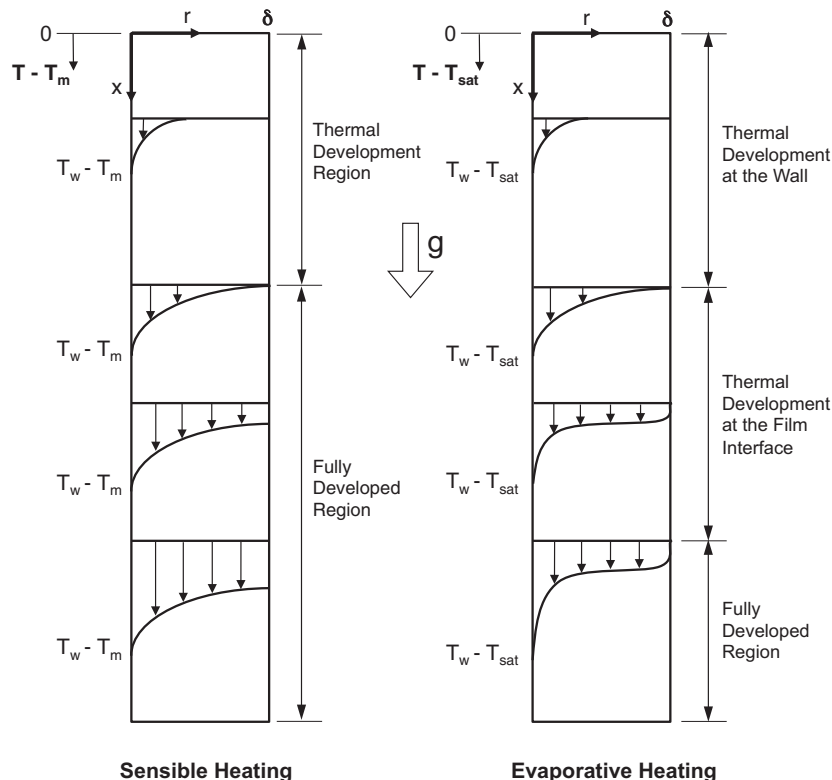


Fig. 12. Differences in thermal development between hydrodynamically fully developed falling films subjected to sensible heating and evaporative heating.

as micro-particle image velocimetry (μ -PIV) [32], must be considered for velocity measurements within the film. Advanced diagnostic tools may also aid in development and validation of computational models for more complex phase change configurations involving wavy interfaces, including annular condensation [33] and flow boiling critical heat flux [34–36].

5. Conclusions

This study examined fluid flow and heat transfer characteristics of turbulent, free-falling liquid film subjected to evaporative heating. A computational model was developed for two-dimensional axisymmetric film flow on a vertical circular tube, with both the computational domain and operating conditions matching those of an experimental database for evaporating water films. Implemented in FLUENT, the model incorporates a phase change model suggested by Tanasawa [14], and is used to predict variations of the evaporative heat transfer coefficient along the heated length, as well as profiles of eddy diffusivity, flow velocity, and temperature across the film. Key findings from the study are as follows.

1. Energy transfer at the film's interface is captured successfully with the aid of the Tanasawa phase change model. An accommodation coefficient of $\gamma = 0.1$ is successful at maintaining the film interface at saturation temperature for all the cases tested.
2. The model predicts variations of the heat transfer coefficient along the heated length similar to those measured experimentally, but with a broader thermal development region.
3. Predicted heat transfer coefficients for a broad range of Reynolds numbers and Prandtl numbers between 3.07 and 5.43 fall between predictions of two prior experimental correlations.
4. The model predicts eddy diffusivity is fully dampened at the film interface. The predicted eddy diffusivity profile resembles the empirical profile recommended by Mudawar and El-Masri [29] for falling films in both trend and magnitude. The predicted velocity profiles follow expected trends.
5. The temperature profile across the liquid film features a steep gradient near the film interface, which is attributed to the dampening of turbulence coupled with energy loss at the film interface.
6. The two-equation $k-\omega$ turbulent model, with shear stress transport (SST) formulation and a turbulence dampening factor of 10 in FLUENT successfully capture the physics of falling films subjected to evaporative heating.
7. This work points to the need for more sophisticated and miniaturized diagnostic tools to measure liquid film thickness, liquid velocity, liquid temperature and turbulence to refine phase change models and further assess the accuracy of computational techniques for study of phase change processes.

Conflict of interest

None declared.

Acknowledgments

The authors are grateful for the partial support for this project from the National Aeronautics and Space Administration (NASA) under grant no. NNX13AB01G.

References

- [1] W. Wilke, *Wärmeübergang an rieselfilme*, VDI Forschungsh. 490 (1962) 1–36.
- [2] G.J. Gimbutis, A.J. Drobacivius, S.S. Sinkunas, Heat transfer of a turbulent water film at different initial flow conditions and high temperature gradients, in: Proc. Sixth Int. Heat Transfer Conf., vol. 1, Toronto, Canada, 1978, pp. 321–326.
- [3] J.A. Shmerler, I. Mudawar, Local heat transfer coefficient in wavy free-falling turbulent liquid films undergoing uniform sensible heating, *Int. J. Heat Mass Transfer* 31 (1988) 67–77.
- [4] N.M. Al-Najem, K.Y. Ezuddin, M.A. Darwish, Heat transfer analysis of preheated turbulent falling films in vertical tube evaporators, *Desalination* 115 (1998) 43–55.
- [5] X. Ye, W. Yan, Z. Jiang, C. Li, Hydrodynamics of free-falling turbulent wavy films and implications for enhanced heat transfer, *Heat Transfer Eng.* 23 (2002) 48–60.
- [6] K.R. Chun, R.A. Seban, Heat transfer to evaporating liquid films, *J. Heat Transfer – Trans. ASME* 93 (1971) 391–396.
- [7] J.A. Shmerler, I. Mudawar, Local evaporative heat transfer coefficient in turbulent free-falling liquid films, *Int. J. Heat Mass Transfer* 31 (1988) 731–742.
- [8] H. Struve, *Der wärmeübergang an einen verdampfenden rieselfilm*, VDI Forschungsh. (1969).
- [9] T. Fujita, T. Ueda, Heat transfer to falling films and film breakdown-II, *Int. J. Heat Mass Transfer* 21 (1978) 109–118.
- [10] F. Gibou, L. Chen, D. Nguyen, S. Banerjee, A level set based sharp interface method for the multiphase incompressible Navier–Stokes equations with phase change, *J. Comput. Phys.* 222 (2007) 536–555.
- [11] R.W. Schrage, *A Theoretical Study of Interphase Mass Transfer*, Columbia University Press, New York, 1953.
- [12] M. Knudsen, *The kinetic theory of gases. Some modern aspects*, Methuen's Monographs on Physical Subjects, London, UK, 1934.
- [13] R. Marek, J. Straub, Analysis of the evaporation coefficient and the condensation coefficient of water, *Int. J. Heat Mass Transfer* 44 (2001) 39–53.
- [14] I. Tanasawa, Advances in condensation heat transfer, in: J.P. Hartnett, T.F. Irvine (Eds.), *Advances in Heat Transfer*, Academic Press, San Diego, CA, 1991.
- [15] W.H. Lee, A pressure iteration scheme for two-phase flow modeling, in: T.N. Veziroglu (Ed.), *Multiphase Transport Fundamentals, Reactor Safety, Applications*, vol. 1, Hemisphere Publishing, Washington, DC, 1980.
- [16] ANSYS FLUENT 12.1 in workbench user's guide, ANSYS Inc., Canonsburg, PA, 2009.
- [17] C.W. Hirt, B.D. Nichols, Volume of fluid (VOF) method for the dynamics of free boundary, *J. Comput. Phys.* 39 (1981) 201–225.
- [18] S. Hardt, F. Wondra, Evaporation model for interfacial flows based on a continuum-field representation of the source terms, *J. Comput. Phys.* 227 (2008) 5871–5895.
- [19] M. Magnini, B. Pulvirenti, J.R. Thome, Numerical investigation of hydrodynamics and heat transfer of elongated bubbles during flow boiling in a microchannel, *Int. J. Heat Mass Transfer* 59 (2013) 451–471.
- [20] J.W. Rose, On interphase matter transfer, the condensation coefficient and dropwise condensation, *Proc. R. Soc. London A* 411 (1987) 305–311.
- [21] O. Kartuzova, M. Kassemi, Modeling interfacial turbulent heat transfer during ventless pressurization of a large scale cryogenic storage tank in microgravity, in: 47th AIAA/ASME/SAE/ASEE Joint Propulsion Conf. & Exhibit, San Diego, CA, 2011.
- [22] N. Mascarenhas, I. Mudawar, Investigation of eddy diffusivity and heat transfer coefficient for free-falling turbulent liquid films subjected to sensible heating, *Int. J. Heat Mass Transfer* 64 (2013) 647–660.
- [23] E.R. Van Driest, On turbulent flow near a wall, *J. Aeronaut. Sci.* 23 (1956) 1007–1011.
- [24] W.M. Kays, Heat transfer to the transpired turbulent boundary layer, *Int. J. Heat Mass Transfer* 15 (1972) 1023–1044.
- [25] W.M. Kays, M.E. Crawford, *Convective Heat and Mass Transfer*, second ed., McGraw-Hill, New York, 1980.
- [26] A.F. Mills, D.K. Chung, Heat transfer across turbulent falling films, *Int. J. Heat Mass Transfer* 16 (1973) 694–696.
- [27] R.A. Seban, A. Faghri, Evaporation and heating with turbulent falling liquid films, *J. Heat Transfer – ASME Trans.* 98 (1976) 315–318.
- [28] G.L. Hubbard, A.F. Mills, D.K. Chung, Heat transfer across a turbulent falling film with concurrent vapour flow, *J. Heat Transfer – ASME Trans.* 98 (1976) 319–320.
- [29] I. Mudawar, M.A. El-Masri, Momentum and heat transfer across freely-falling turbulent liquid films, *Int. J. Multiphase Flow* 12 (1986) 771–790.
- [30] I. Mudawar, R.A. Houpt, Mass and momentum transport in smooth falling liquid films laminarized at relatively high Reynolds numbers, *Int. J. Heat Mass Transfer* 36 (1993) 3437–3448.
- [31] I. Mudawar, R.A. Houpt, Measurement of mass and momentum transport in wavy-laminar falling liquid films, *Int. J. Heat Mass Transfer* 36 (1993) 4151–4162.
- [32] W. Qu, I. Mudawar, S.-Y. Lee, S.T. Wereley, Experimental and computational investigation of flow development and pressure drop in a rectangular microchannel, *J. Electron. Packag.* – Trans. ASME 128 (2006) 1–9.
- [33] H. Lee, I. Mudawar, M.M. Hasan, Experimental and theoretical investigation of annular flow condensation in microgravity, *Int. J. Heat Mass Transfer* 61 (2013) 293–309.
- [34] J.C. Sturgis, I. Mudawar, Critical heat flux in a long, rectangular channel subjected to onesided heating – I. Flow visualization, *Int. J. Heat Mass Transfer* 42 (1999) 1835–1847.
- [35] J.C. Sturgis, I. Mudawar, Critical heat flux in a long, rectangular channel subjected to onesided heating – II. Analysis of critical heat flux data, *Int. J. Heat Mass Transfer* 42 (1999) 1849–1862.
- [36] C. Kharangate, I. Mudawar, M.M. Hasan, Experimental and theoretical study of critical heat flux in vertical upflow with inlet vapor void, *Int. J. Heat Mass Transfer* 55 (2013) 360–374.